Poly(dicarbon monofluoride) $(C_2F)_n$ bridges the neutron reflectivity gap

Valery Nesvizhevsky[1*], Killian Henry[2,3], Louise Dauga[2], Batiste Clavier[2], Sylvie Le Floch[4], Egor Lychagin[5], Alexei Muzychka[5], Alexander Nezvanov[5], Vittoria Pischedda[4], Cole Teander[6], Kylyshbek Turlybekuly[5,7,8], Silvana Radescu[8], Brigitte Vigolo[3], Sébastien Cahen[3], Claire Hérold[3], Jafaar Ghanbaja[3], Kirill Zhernenkov[5], Marc Dubois[2,*]

[1]Institut Max von Laue – Paul Langevin, 71 avenue des Martyrs, F-38042, Grenoble, France

[2]Université Clermont Auvergne, CNRS, Clermont Auvergne INP, ICCF, 24, avenue des Blaise Pascal, 63178 Aubière, France

[3]Université de Lorraine, CNRS, Institut Jean Lamour, UMR 7198, allée André Guinier 54000 Nancy, France

[4]Institut Lumière Matière, UMR5306 – UCBL – CNRS, 10 rue Ada Byron, 69622 Villeurbanne CEDEX, France

[5]Frank Laboratory of Neutron Physics, Joint Institute for Nuclear Research, 6 Joliot Curie, Ru-141980 Dubna, Russia

[6]Department of Nuclear Engineering, North Carolina State University, Raleigh, NC 27695, USA

[7]The Institute of Nuclear Physics, Ministry of Energy of the Republic of Kazakhstan, Ibragimova Str. 1, Almaty 0500032, Kazakhstan

[8] Departamento de Física and Instituto de Materiales y Nanotecnología, MALTA Consolider Team, Universidad de La Laguna, E38200 San Cristóbal de La Laguna, Tenerife, Spain

Abstract

Graphites covalently intercalated with fluorine to form $(C_2F)_n$ structural type compounds shows a dramatic increase of the interlayer distance up to by a factor of almost 3 to reach ~9 Å. Such graphite fluoride compounds containing only carbon and fluorine offer the rare opportunity to bridge the so-called gap in the reflectivity of neutron reflectors. Slow neutron reflectors are of great interest in designing neutron sources as well as in fundamental and

* nesvizhevsky@ill.eu
marc.dubois@uca.fr

applied science; they require synthesizing high thermal and chemical compound stability graphite fluorides. In this work, a new strategy is proposed for synthesizing $(C_2F)_n$ compounds in a well-controlled method. Our results show that the outcome $(C_2F)_n$ has a covalent character with only sp^3 hybridized carbon atoms. Moreover, C-F bonds in the fluorocarbon sheets and CF_2 groups on the sheet edges lead to the desired stability and hydrophobic character. A dedicated home-made neutron diffractometer was built for measurements of double-differential neutron cross sections of crystals with specific large interlayer distances found in $(C_2F)_n$ compounds. We demonstrate that the synthesized fluorine intercalated graphites developed effectively cover the gap in the reflectivity for the new generation of neutron reflectors.

1. Introduction

For many decades, neutrons have been an indispensable tool for studying matter and fundamental interactions.[1-8] The most intense neutron sources, based on high-flux nuclear reactors or accelerator-driven spallation sources, are usually built and operated by several countries and serve thousands and tens of thousands of users to conduct research in a variety of science fields. Thus, in Europe, examples of such user facilities are Institute Laue Langevin (ILL), Grenoble, France (nuclear reactor) and European Spallation Source (ESS), Lund, Sweden (spallation source). In both cases, the initial neutron energy is on the order of MeV, while most applications require thermal and colder neutrons. Therefore, the second fundamentally important element of a neutron source is the moderator/reflector (these two functions can be combined in one substance or separated).

The efficiency of thermal neutron reflectors is quite high. In particular, it was this property of graphite that made it possible to design the first nuclear reactor in 1942 at the University of Chicago under the leadership of Enrico Fermi[9]. Graphite reflectors continue to be used in the construction of nuclear reactors today. However, the efficiency of standard

neutron reflectors, like graphite, decreases sharply at neutron energies below the so-called Bragg cutoff[10] associated with the coherent scattering of neutrons on crystal planes. The value of the energy depends on the reflector material; the neutron wavelength λ_n corresponding to this energy value is equal to 2 interplanar distances d ($\lambda_n = 2 \cdot d$). For graphite[11], it is $\lambda_n^{Bragg(Gr)} = 2 \cdot d_G = 6.708\ \mathring{A}$, (where $d_{Gr} = 3.354\ \mathring{A}$).

The reason for this drop in the efficiency of reflectors is quite fundamental and is due to the wave properties of the neutron. If λ_n is greater than the characteristic distance between atoms in a substance, the neutron does not distinguish the nuclei of the substance and penetrates through the substance without intense scattering. To overcome this limitation for the slowest neutrons, we have developed a reflector method based on fluorinated detonation nanodiamond (F-DND) powders.[12-16] The role of interatomic distances is played by the distance between the centers of nanoparticles.[12] With the very high efficiency of such reflectors for the slowest neutrons (approaching 100 %), the efficiency drops to 80-90 % and below as the wavelength λ_n decreases to a value of the order of $\lambda_n^{F-DND} \sim 18 - 20$ Å[17-19], for reasonable reflector thicknesses. Thus, in the neutron wavelength range $\left[\lambda_n^{F-DND} - \lambda_n^{Bragg}\right]$ there is still a gap in reflectivity, only partially covered with less efficient materials[20].

Some of the applications would be to design more efficient neutron sources with record phase-space densities based on such reflectors and cryogenic moderators, and to increase the efficiency of neutron production and delivery from conventional sources to experimental facilities. Increased fluxes of cold neutrons (CN) and very cold neutrons (VCN) are of great interest for a number of standard neutron scattering techniques and particle physics experiments. The authors' biased list for the applications of VCN includes an increase in the sensitivity of experiments to search for neutron-antineutron oscillations[21-23] and short-range fundamental forces[24,25], neutron spin-echo techniques[26-28] and interferometers[29,30], increasing the non-specular reflection signal of neutron reflectometers and reducing the

thickness of samples for small-angle scattering, tomography[31]. The variety of applications of CN is well-known and does not need justification. Finally, a principal possibility of obtaining record-breaking pulses of cold and thermal neutrons of nearly the same phase-space density from low-power neutron sources[32,33] has to be explored.

In order to fill the reflectivity gap of very slow neutrons, we have developed in this work a new type of reflectors. They are based on Bragg scattering exactly as in the case of conventional graphite, however, with significantly larger interplanar distances. We chose graphite fluoride (GF) as such a crystal for the following reasons. It consists of atoms with very small capture cross sections ($\sigma_{abs}^{C} = 3.5\,mb$ and $\sigma_{abs}^{F} = 9.6\,mb$ at the thermal neutron velocity, respectively) and large coherent scattering length ($b^{C} = 6.65\,fm$ and $b^{F} = 5.65\,fm$, respectively). Graphite is relatively free from impurities and can be further purified to a significant extent.[34] Interplanar distances in GF can be dramatically increased compared to pristine graphite, up to by a factor of ~3. Moreover, they can be optimized for specific applications by selecting fluorination conditions or applying moderated external pressure[35]. Two other reasons are related to the intrinsic properties of GF: i) their high thermal and chemical stabilities and ii) their hydrophobicity.

The compounds which combine carbon and fluorine elements can be classified in two types: fluorine graphite intercalation compounds (F-GICs) usually denoted C_xF and graphite fluorides, CF_x. Although its high reactivity, pure gaseous molecular fluorine (F_2) reacts with graphite only when the temperature is higher than 350°C.[36-41] Nevertheless, F-GICs are synthetized at temperature lower than 100 °C thanks to volatile fluorides or their mixture HF, IF_5, BF_3, WF_6, …. Molecular fluorine F_2 can be added in the catalytic mixture in order to increase the reactivity and then the content of intercalated fluorine. Because of the low fluorination temperature, the resulting C-F bonding in F-GICs is in between ionic and weakened covalent character (rather than semi-covalent or semi-ionic).[42-45] The C-F bonds are

then less stable in F-GICs than in covalent graphite fluorides prepared at high temperature (350-650 °C under pure F_2 gas).

So, in the present work the latter compounds with the highest thermal and chemical stabilities are considered in order to avoid changes under high radiation fluxes and at high temperatures that might be associated with the operation of such neutron reflectors. Moreover, covalent bonds and CF_2 groups on the sheet edges are responsible for the hydrophobic character of GF. Such a property is of primary importance for the reflection of slow neutrons because it avoids physisorption of water molecules. Hydrogen in those molecules must be absent in the reflector because of its capture cross section of $\sigma_{abs}^{C} = 33\ mb$ and huge inelastic scattering cross sections.

Among covalent GF, two structural phases exist. *Poly(carbon monofluoride)* $(CF)_n$ with composition $CF_{0.92}$ was first synthesized by Ruff and Bretschneider[46]. The works by W. Rüdorff and G. Rüdorff in between 1947 and 1959 were then related to GF with compositions $CF_{0.68}$ to $CF_{0.995}$.[47] In 1979, *poly(dicarbon monofluoride)* $(C_2F)_n$ has been discovered par Kita *et al.*[48]. The interlayer distance *d* in $(CF)_n$ and $(C_2F)_n$ types allows us to select the latter as the most efficient for the neutron reflection. Whereas each carbon atom is fluorinated in $(CF)_n$ resulting in a FCF/FCF stacking sequence with an interplanar distance *d* equal to 6 Å, half of the carbon atoms is bound to fluorine in $(C_2F)_n$ phase. So, the stacking sequence is FCCF/FCCF and *d* = 9 Å (Fig. 1). The higher the content of $(C_2F)_n$ phase in GF, the higher the efficiency of the reflector for neutrons. The synthesis of pure $(C_2F)_n$ phase is challenging because it is an intermediate compound before the completion of the fluorination and the formation of $(CF)_n$ type stating from graphite. According to Kita *et al.*[49], the fluorination temperature must be ranged in between 350 and 400 °C. The reaction duration must be longer enough to promote fluorine diffusion and avoid residual graphitic regions. As fluorination is a heterogeneous gas/solid reaction, a higher fluorination rate could be reached in the outer parts

of the grain. Moreover, the addition of F_2 gas must be controlled in order to avoid the partial exfoliation of the fluorocarbon sheets. Our aim for neutron reflection needs materials as dense as possible and the partial exfoliation results in both structural disorder and the decrease of the density. Our strategy lies in two points: i) the use of graphites with large grain size (44 and 200-400 µm) in order to slow down the conversion of $(C_2F)_n$ into $(CF)_n$ type thanks to the limitation in the fluorine diffusion and ii) long fluorination duration, *i.e.* 72 h (see experimental part), for the completion of the graphitic phase fluorination. The neutron reflection measurements need high quantities of GF and the process must be up-scalable. A minute control of both the fluorination temperature increase and the addition of fluorine gas are mandatory.

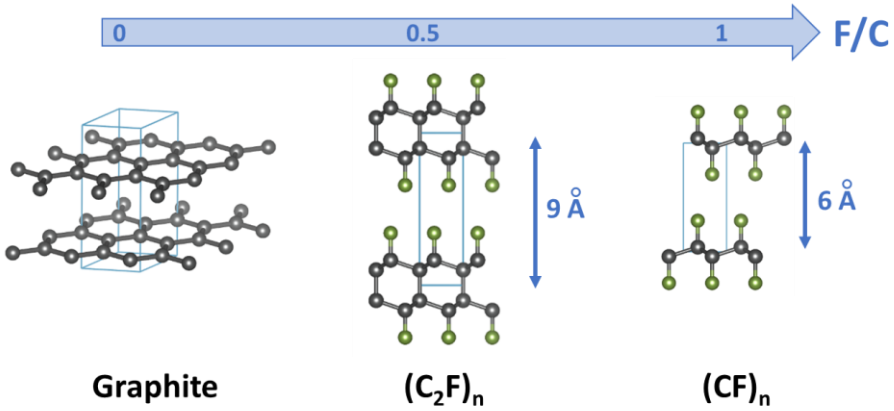

Figure 1. Structures of graphite, *poly(dicarbon monofluoride)* $(C_2F)_n$ and *poly(carbon monofluoride)* $(CF)_n$

2. Experimental

2.1. Fluorination of graphite

The graphite fluorides were first prepared from a Timrex KS44 graphite with 44 µm grain size through a direct fluorination process using pure gaseous molecular fluorine, F_2. The second sample was natural graphite NG (Sigma Aldrich) with small flakes of 200-400 µm

lateral size and 1-150 μm thick. An up-scalable static mode was used to perform the fluorination for 72 h in a 5 L tubular reactor made of nickel alloy and passivated with NiF_2. In this mode, fluorine was added in a closed reactor starting from primary vacuum (10^{-3} mbar). 5 g of graphite were located onto 2 plateaux. Before the reaction, moisture and oxygen were removed by applying a primary vacuumm (10^{-3} mbar) at 200 °C. Figure 2 displays the process with pulsed addition of F_2 gas.

In order to determine the fluorination temperature, the fluorine pressure was recorded as a function of the time and temperature (Fig. 2). As discussed in the introduction part, the reactive gas was added at 200 °C, a temperature at which no reaction occurs. The first temperature step was 270 °C without reaction. At 360 °C, F_2 was slightly consummed in accordance with Kita's "$(C_2F)_n$ rich" region, *i.e.* 350-400 °C. The fluorine pressure droped at 430° C sign of a drastic fluorination. The high granulometry of KS44 graphite shifted the fluorination temperature in comparison with Kita's work: "$(C_2F)_n$ rich" region[48]. F_2 gas was added to compensate its consumption. 430 °C was maintained for 16 h before multi-step increase up to 600 °C for annealing purpose.

Taking into account those data, a series of two-step fluorinations for both KS44 and NG graphites was carried out as follows: after the preliminary step (primary vacuum at 200 °C, addition of F_2 at 270 °C, step at 360 °C for 2 h), the reaction temperature was first maintained at 450°C for 24 h to form the $(C_2F)_n$ phase and then increased to T_F (450, 550 and 610 °C) to enhance the structural homogeneity by annealing. The annealing temperature was maintained for 24 h. For T_F = 520 °C, the duration is only 18 h for technical reason. The samples are denoted F450-KS, F520-KS, F550-KS, F610-KS for KS44, and F440-NG for NG, respectively; F for flurination is followed by the reaction tempearture and KS44 and NG are the starting samples. Only for this latter starting sample and according to the characterization data the fluorination temperature was maintained at 410°C for 48 h and the

sample is denoted F410-NG. Addition of F_2 gas was performed when the pressure drop was at least of 0.2 bar. After the fluorination reaction and during the cooling of the reactor, the reactive atmosphere was flushed with nitrogen gas.

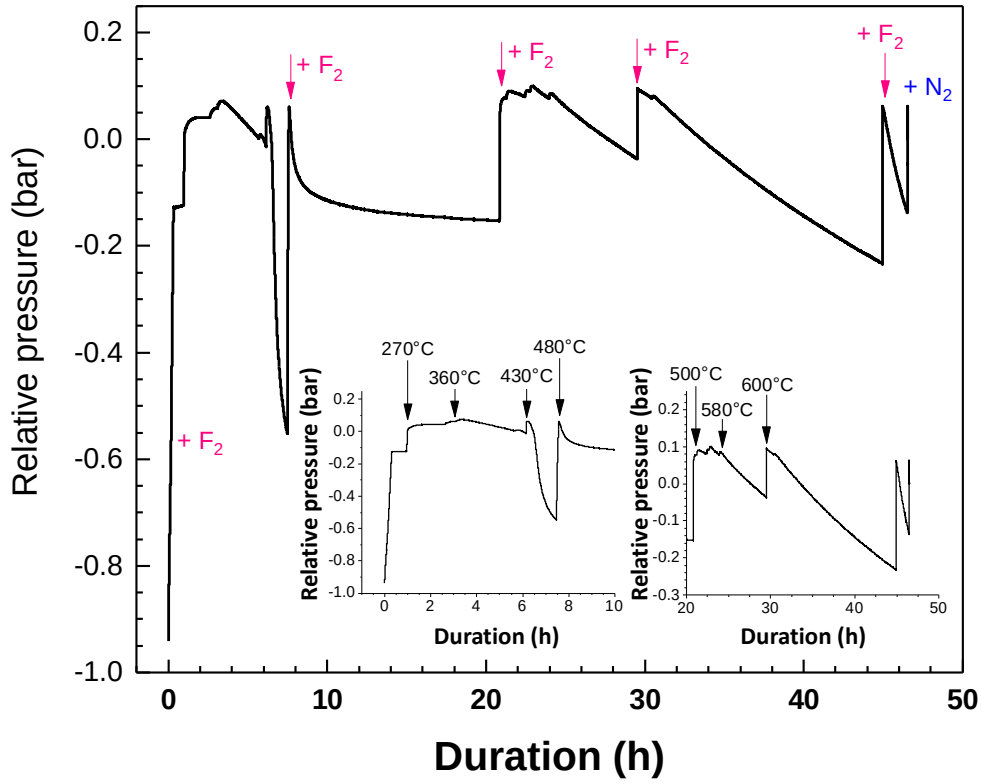

Figure 2. Pulsed additions of F_2 gas and monitoring of the fluorination temperature.

2.2. Physicochemical characterization

^{19}F and ^{13}C solid-state nuclear magnetic resonance (NMR) spectra were acquired on a Bruker AVANCE spectrometer. 2.5 mm zirconia rotors rotating at 30 kHz were used. For MAS (magic angle spinning) spectra, a simple sequence was performed with a single $\pi/2$ pulse length of 4.0 and 3.5 μs for ^{19}F and ^{13}C, respectively. ^{13}C NMR was performed at a frequency of 73.4 MHz and tetramethylsilane (TMS) was used as the reference. ^{19}F NMR was

carried out with a frequency of 282.2 MHz and the spectra were externally referenced to $CFCl_3$.

Fourier-transform infrared (FTIR) spectra were recorded on a Nicolet 6700 FT-IR (Thermo scientific) spectrometer in transmission mode at 4 cm^{-1} resolution and 256 scans were taken for each spectrum.

X-ray diffractograms were recorded on a Bruker D8 Advance diffractometer using a molybdenum anticathode ($\lambda_{K\alpha 1}$ = 0.70930 Å) and equiped with a 2D LynxEye detector and a 2.5° divergence Soller slit. The recorded spectra were accumulated for 1 h in a 2-45 ° (2θ) angular range, repeated 8 times in order to increase the signal-to-noise ratio. Samples were placed in Lindemann glass capillaries (1.5 mm diameter) and rotated at 10 rpm in order to minimize the preferential orientation.

For TEM and High Resolution TEM (HRTEM) analysis, F-KS44 was dispersed in ethanol under sonication during 15 min. One droplet of the dispersion was deposited on a 200-mesh-size holey carbon grid provided by Delta Microscopies. The TEM observations were carried out using a JEOL ARM 200F cold FEG apparatus (operating voltage of 80 kV) equipped with a nitrogen liquid-cooling (-175 °C) sample holder.

2.3. DFT calculations

The details of the Density Functional Theory (DFT) simulations performed for the study of the C_2F system in sp^3 hybridization (in both bulk and slab form), in sp^2-sp^3 hybridization [composed by (CF)n-type structure within intercalated graphene layers] and of bulk CF are similar to those of previous work[35,50] We used the Vienna Ab Initio Simulation Package (VASP) computational code, which implements the projector-augmented wave

method (PAW), with the Perdew-Burke-Ernzerhof (PBE) generalized gradient approximation (GGA), including dispersive corrections within the so-called Grimme's D2 scheme[51-55]. The cutoff in the plane waves basis set was taken at 600 eV. For the study of the lattice vibrations, we used the density functional perturbation theory (DFPT, or linear-response method) as implemented in the VASP code, using the Phonopy package to calculate the phonon density of states[56].

2.4. Special neutron diffractometer

In order to characterize the produced samples in terms of the efficiency of such reflectors, a specialized diffractometer was home-designed. The reason is that standard diffractometers typically use neutron wavelengths outside the range of our interest (we are interested in wavelengths well above $\lambda_n^{Bragg(Gr)}$), and/or they do not allow measurements of different wavelengths over a wide range, and/or they do not allow measurements of scattered neutrons at nearly all angles. The details are given in Appendix 1 of supplementary information.

3. Results and discussion

3.1 *Towards a pure $(C_2F)_n$ phase*

A F/C molar ratio close to 0.6 was obtained by weight uptake for the GF starting from KS44 and NG whatever the temperatures of fluorination and annealing; the value is slightly higher than the value expected for the $(C_2F)_n$ phase (F/C = 0.5). This is the first indication of the preparation of a majority $(C_2F)_n$ phase.

First, solid state NMR allows the investigation of the structural type at the short range order. ^{13}C NMR spectrum of a perfect $(C_2F)_n$ phase is theoretically composed of only two lines with equal integrated surfaces and assigned to carbon atoms involved in C-F bonds

(denoted C-F in Fig. 3) and non-fluorinated carbons with sp^3 hybridization (C-C-F), their chemical shifts are 84 and 42 ppm, respectively[54,57-60]. CF_2 groups are evidenced with a line at 110 ppm. Their content is expected very low in GF with large lateral size such as those obtained from KS44 and NG. Considering ^{19}F nuclei, only one line is expected for a perfect $(C_2F)_n$; phase at -176 ppm for covalent C-F bonds (C-F). A minor component at -120 ppm can be recorded because of the presence of CF_2 groups.

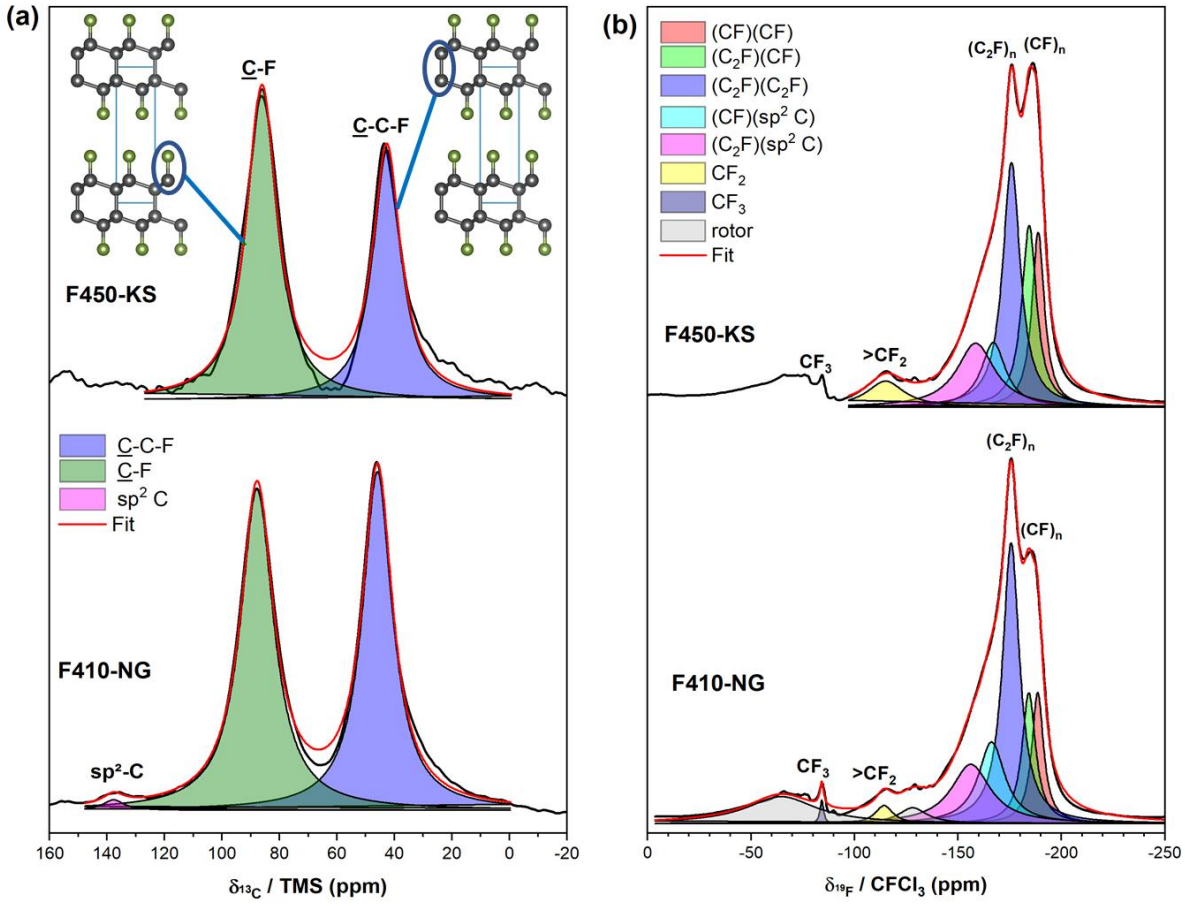

Figure 3. MAS NMR spectra of F450-KS and F410-NG on ^{13}C (a) and ^{19}F nuclei (b). The spinning rate is 10 and 30 kHz, respectively.

Solid-state ^{13}C MAS NMR of F450-KS reveals the absence of sp^2 hybridized carbon atoms in the sample which signature is expected in the 130-140 ppm[40,43,57-61] range (Fig. 3a).

CF_2 are negliegable since no line is observed at 110 ppm[40,43,57-61]. The lines at 42 ppm (C-C-F) and 84 ppm (C-F) are observed with different integrated surfaces. The content of C-F bonds is higher than that expected for $(C_2F)_n$, the resulting excess is explained by the formation of $(CF)_n$ phase. C-F bonds exhibit similar chemical shift in $(C_2F)_n$ and $(CF)_n$, *i.e.* 84 ppm[61]. The performed fitting of the spectra allows to evaluate the ratio of two phase contents. According to the integrated surface of the lines S_{C-F} and S_{C-C-F}, the formula $100*(C_2F)_n/(CF)_n = 100*S_{C-C-F}/S_{C-F}$ was used to calculate the percentage of $(C_2F)_n$ structural type. 76 % of C-F bonds are included in the $(C_2F)_n$ structural type (24 % in $(CF)_n$). Moreover, the F/C ratio can be extracted from the fits thanks to the formula $F/C= S_{C-F}/(S_{C-F} + S_{C-C-F})$, where it remains constant around 0.50-0.60 regardless of the fluorination and annealing temperatures (see Fig. SI2a and Table SI1 in supplementary information) and in good agrement with the weigth uptake method. The $\%(C_2F)_n$ is 70 %, 72 % and 67 % for F520-KS, F550-KS and F610-KS, respectively. The higher the annealing temperature, the higher the content of $(CF)_n$ type. The shorter fluorination duration for F520-KS 18 h explains the slightly higher $\%(C_2F)_n$.

The case of ^{19}F spectra is more complex since 5 lines are recorded in addition to the minor ones of CF_2 (-120 ppm) and CF_3 (-80 ppm) instead of one expected (Fig. 3b)[57,58,61,62]. Differences appear according to the fluorination and annealing temperatures (Fig. SI2b). When those temperatures increase, the integrated surfaces of the lines at -160 and -168 ppm decrease. Those lines are assigned to ^{19}F in C-F bonds in $(C_2F)_n$ and $(CF)_n$ types with non-fluorinated sp^2 carbon in their neighboring, denoted $(C_2F)(Csp^2)$ and $(CF)(Csp^2)$ for lines at -160 and -168 ppm, respectively. ^{13}C data (Fig. 3a, SI1a and SI2a) evidence the presence of $(CF)_n$ regions and the corresponding chemical shift is the lowest (the more negative); so the line at -190 ppm is assigned to the C-F bonds in $(CF)_n$ (CF)-(CF). The two last lines are related to C-F bonds in $(C_2F)_n$ with C_2F ($(C_2F)_n$) and CF ($(CF)_n$) neighborings at -178 ppm (noted $(C_2F)(C_2F)$) and -183 ppm ($(C_2F)(CF)$), respectively. This assignement is in perfect

aggreement with the chemical shift at -178 ppm of fluorinated nanodiamonds, *i.e.* Csp^3-C<u>F</u> (the ^{13}C chemical shift is 42 ppm)[15]. Fig. 3b summerizes the above assigments with the notation (C_2<u>F</u>)(Csp^2), (C<u>F</u>)(Csp^2), (C_2<u>F</u>)(C_2F), (C_2<u>F</u>)(CF) and (C<u>F</u>)(CF). The content of (C_2<u>F</u>)(C_2F) is nearly constant (Fig. SI2b) and increasing the fluorination and annealing temperatures increase the contents of (C_2<u>F</u>)(CF) and (C<u>F</u>)(CF).

For the best of our knowledge, all the components of ^{19}F NMR in $(C_2F)_n$-rich GF are assigned for first time. The high content of $(C_2F)_n$ phase (76 %) is confirmed at the short range order. To go further with our strategy that involves graphite-based compounds with large lateral size (KS44 with 44 μm grain), natural graphite flakes (NG with 200-400 μm lateral size) were fluorinated at 430 °C for 24 h and annealed 24 h at 440 °C (F440-NG). ^{13}C spectrum reveals 94 % of $(C_2F)_n$ phase in F440-NG (Fig. SI3a and table SI1). For the sample with the higher content of $(C_2F)_n$ phase, *i.e.* 96 % was achieved with a fluorination carried out at 410 °C for 48 h (Fig. 3). With such content, the amounts of residual sp^2 C and C-F in $(CF)_n$ are low, as well as the components (C_2<u>F</u>)(Csp^2), (C<u>F</u>)(Csp^2), (C_2<u>F</u>)(CF) and (C<u>F</u>)(CF). The corresponding ^{19}F spectrum is dominated by the (C_2<u>F</u>)(C_2F) component (-178 ppm) in perfect line with our assigments. Another observation is consistent with these findings: (C_2<u>F</u>)(CF) and (C<u>F</u>)(CF) exhibit nearly the same integrated structure because they are both related to the content of $(CF)_n$.

For both FT_F-KS and FT_F-NG series (T_F is the fluorination temperature), the increase of the annealing temperation does not increase the content of $(C_2F)_n$ phase, *i.e.* around 72 and 95 % for FT_F-KS and FT_F-NG series, respectively (Fig. SI2 and SI3 and Table SI1). On the contrary, when the annealing temperature is increased to 610 °C, the content of $(C_2F)_n$ phase decreases down to 67 % in both series. In that case, the percentage of $(C_2F)_n$ region converted to $(CF)_n$ increased, probably close to the material surface.

As revealed by NMR, the samples exhibiting close short range order with mainly $(C_2F)_n$ as structural phase, X-ray diffraction (XRD) was performed with selected samples (F450-KS and F-NG-440) ; the patterns are given in Figure 4. Both samples exhibit five diffraction peaks localized at the same position. The two first peaks are indexed as (001) and (002) planes, while the remaining peaks are due to (hk0) planes: (100), (110) and (200) at 2.18, 1.28 and 1.09 Å, respectively. Because of the scattering at low angles masking partially the (001) peak, the position of the (002) diffraction peak was used to determine the interplanar distance in the synthesized $(C_2F)_n$. The obtained d-spacing of F450-KS and F440-NG are of 9.0 and 9.2 Å, respectively, in agreement with the literature[63,64]. Even though $(CF)_n$ phase was evidenced by NMR spectra, no overlap of the 00*l* peaks of $(CF)_n$ is observed (expected at 6 Å for (001) plane). [37,40,41] XRD results evidence the obtaining of a quasi $(C_2F)_n$ single phase in the long range order. No significant difference between samples can be noted regarding their crystallinity, as peak widths and positions of the *hk*0 reflections remain quite similar.

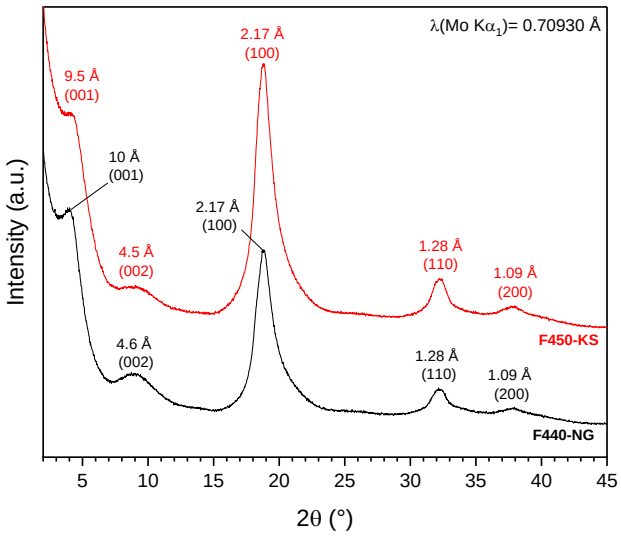

Figure 4. XRD patterns of fluorinated graphite prepared from pristine KS44 at 450 °C (red) and NG at 440 °C (black) respectively. A Mo Kα source was used (0.70930 Å).

Thus, regardless of the starting graphite (KS44 or NG), the XRD patterns corresponding to fluorinated graphite can be indexed as $(C_2F)_n$ phase and no other diffraction peak seems to be necessary to fully assign the observed features. No diffraction peak corresponding to pristine graphite or $(CF)_n$ phase is observed.

The TEM investigations performed on F450-KS are presented in Figure 5. Figure 5a shows a typical single foil deposited on the TEM holey grid and the observations have been focused on the edges of the F450-KS foils. Multiple-layer sheets could be well observed in Figures 5b and 6c, being a magnified area of the image shown in Figure 5b. The HRTEM image (Figure 5c) allows to perform a Fast Fourier Transform (FFT) image (insert), represented by the yellow area on the edge of the observed foil in Figure 5c. The FFT image exhibits four diffraction spots which are attributed to the lattice planes (001) of $(C_2F)_n$, (001) of $(CF)_n$ and the (002) and (004) planes of the $(C_2F)_n$ structure. The interlayer spacing is estimated to be of 8.59 Å, 5.30 Å, 4.23 Å and 2.12 Å, respectively. In order to confirm the FFT indexation, profile lines were drawn on two areas of the foil: i) the extreme edge (blue) and ii) an area further away from the edge of the foil (green). The layer spacing measured is shown in Figure 5d. The edges at the flake extremity seem to be terminated by a few $(CF)_n$ layers since a d-spacing of 5.94 Å is measured. This profile line measurement confirms the presence of the (001) plane of $(CF)_n$ in the FFT image, which is certainly favorized at these zones where F_2 diffusion is easier. This could explain the presence of $(CF)_n$ type in the ^{19}F NMR spectra (Figure 3b). Conversely, the inside of the foil is constituted of the $(C_2F)_n$ phase where multiple d-spacing is observed, ranging from 8.54 Å to 10.24 Å. The XRD peaks broadening could be explained by these interlayer distances. Fluorination results in a partial exfoliation located at sheet edges that may explain the highest d-spacing. For several other investigated regions, not shown, the same outcome with a major $(C_2F)_n$ phase and small fractions of $(CF)_n$ at the foil edges is obtained.

From TEM, d-spacing profile lines and FFT are in very good agreement with XRD results showing that the experimental conditions used for fluorination of KS44 and NG lead to synthesize of the stable $(C_2F)_n$ phase.

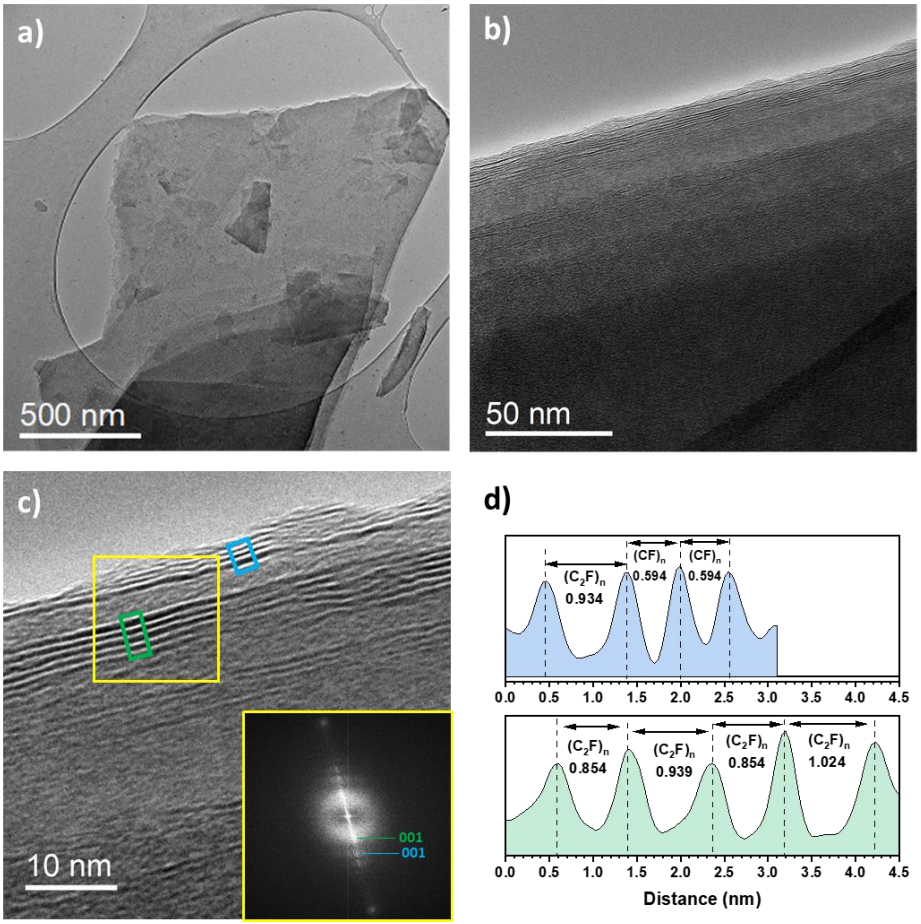

Figure 5. TEM images of the F450-KS sample showing a single foil deposited on the TEM holey grid (a) and the edge of another foil (b). (c) is an HRTEM image of the edge of the foil presented in (b), with corresponding FFT image (insert) taken on the yellow area and associated profile lines of the edge (green rectangle) and the extreme edge (blue rectangle) of the foil (d). Blue is associated to $(CF)_n$ structure while green stand for $(C_2F)_n$.

F440-NG can then be considered as a quasi-perfect $(C_2F)_n$ phase whereas the series for KS44 are rich-$(C_2F)_n$ compounds. The assignment of the infrared (IR) spectra can be up-dated in comparison with the literature. The IR spectrum of F450-KS and its decomposition are shown in Fig. 6. The vibration of covalent C-F bonds is located at around 1220 cm^{-1} for both

phases[34,49,58,60-62]. The spectrum is characterized by strong vibrational bands at 1350 and 940 cm^{-1}. This band is assigned in the literature to antisymmetric elongation of $>CF_2$ groups[65]. Its intensity is not compatible with this attribution. As a matter of fact, CF_2 groups are only possible at the edges of sheets (C-F only in the fluorocarbon sheets). In conventional graphite, carbons at the sheet edges are negligible compared with those in the sheets. Conversely, the band visible at 1075 cm^{-1} in the spectrum of the $(CF)_n$ phase corresponds to the symmetrical elongation of $>CF_2$ groups[47-53]. The bands at 1350 and 940 cm^{-1} are strongly related to the $(C_2F)_n$ phase. To confirm this hypothesis, DFT calculations were performed. Additionally, IR spectra of different annealing temperature were acquired for the FT_A-KS series (Fig. SI4) and the same bands than those of F450-KS are observed.

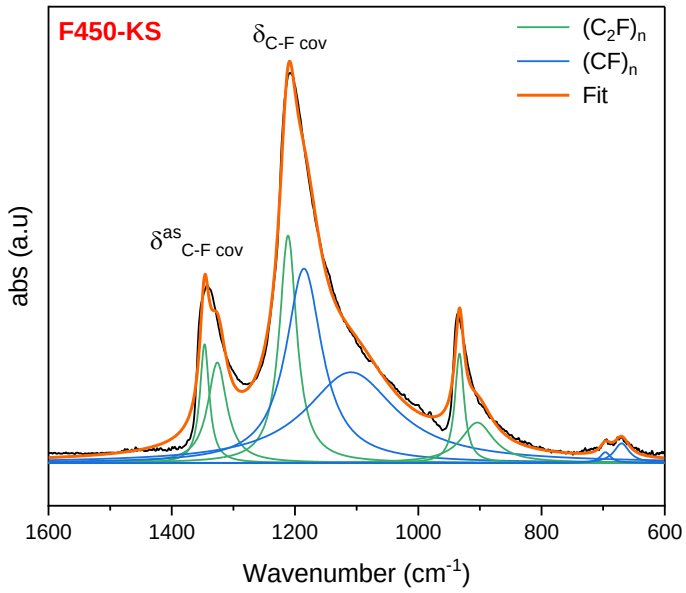

Figure 6. IR spectrum of F450-KS. Decomposition on the spectrum (black) was achieved by nine Lorentzian profiles, with $(C_2F)_n$ and $(CF)_n$ in green and blue, respectively, while the resulting sum of the fitted curves is in orange.

Figure 7 shows the calculated vibrational density of states (DOS) for the C_2F–sp^3 system as bulk and slab form (a, top) and for the CF and C_2F systems in sp^2- sp^3 hybridization (b, bottom).

At low frequencies (up to about 500 cm^{-1}) and for both materials, the contribution of the F atoms (green curve) is dominant over that of the C atoms (black), with the opposite behavior at high frequencies, for which the phonon peaks correspond mainly to carbon atoms.

CF (where each carbon atom is bonded to one fluorine atom) and the C_2F -sp^2 - sp^3 form (composed by intercalated layers of CF and graphene) show similar characteristics, with a strong interaction among these atoms at intermediate domain frequencies (between 500 cm^{-1} and 750 cm^{-1}), as seen in Figure 7b).

The mechanical representation of the CF and C_2F–sp^3 (bulk and slab) hexagonal structures (with space group No. 164, P-3m1) yield similar multiplicities for the irreducible representations of the modes at the zone center: $n\ A_{1g}\ (R) + n\ E_g\ (R) + n\ A_{2u}\ (IR) + n\ E_u\ (IR)$, where R indicates Raman-active modes, IR indicates infrared active modes and n (multiplicity factor) has the value 2 (CF), 3 (bulk C_2F – sp^3) and 9 (C_2F – sp^3 slab). The positions of the calculated vibrational modes are represented by colored tick marks in Figure 7.

For the C_2F sp^2-sp^3-hybridized form (space group No. 1), the mechanical representation for the irreducible modes is 36A where all A modes are both Raman and infrared active, as represented by pink ticks in Figure 7 (b). The vibrational modes around 1300 cm^{-1} correspond to contributions of the CF layer, whereas the modes at frequencies around 1450 cm^{-1} correspond only to vibrations of the carbon atoms of sp^2 hybridization (graphene layer).

An exhaustive analysis of the eigenvectors involved in the vibrations of each mode has been carried out. Of special interest is the study of the A_{2u} infrared mode, corresponding to the contribution of the C-F bond vibration. Figure SI5 shows the calculated intensities of the

IR spectra for the structures with hexagonal symmetry, where the peaks correspond to the frequencies of the irreducible modes A_{2u} and E_u.

The peaks corresponding to A_{2u} (red ticks in Figure 7) are assigned to antisymmetric C-F stretching modes, whose values are very close to those observed experimentally. For bulk structures with hexagonal symmetry, the following values are obtained for the A_{2u} modes: 1153 cm^{-1} (CF), 917 cm^{-1} and 1287 cm^{-1} (bulk C_2F-sp^3).

The slab structure contains mostly both bulk modes and those associated with surface effects, as it can be seen from the ticks in Figure 7a. From the intensities of the peaks of the IR spectrum in Figure SI5 one sees that the relevant A_{2u} modes involved in the vibration, are those corresponding to frequencies 450, 936, 954, 1150, 1319, and 1344 cm^{-1}, with the largest intensity found for the modes at 936 and 450 cm^{-1}. The results obtained for the IR A_{2u} modes, 1344 and 936 cm^{-1}, are in good agreement with the experimental data.

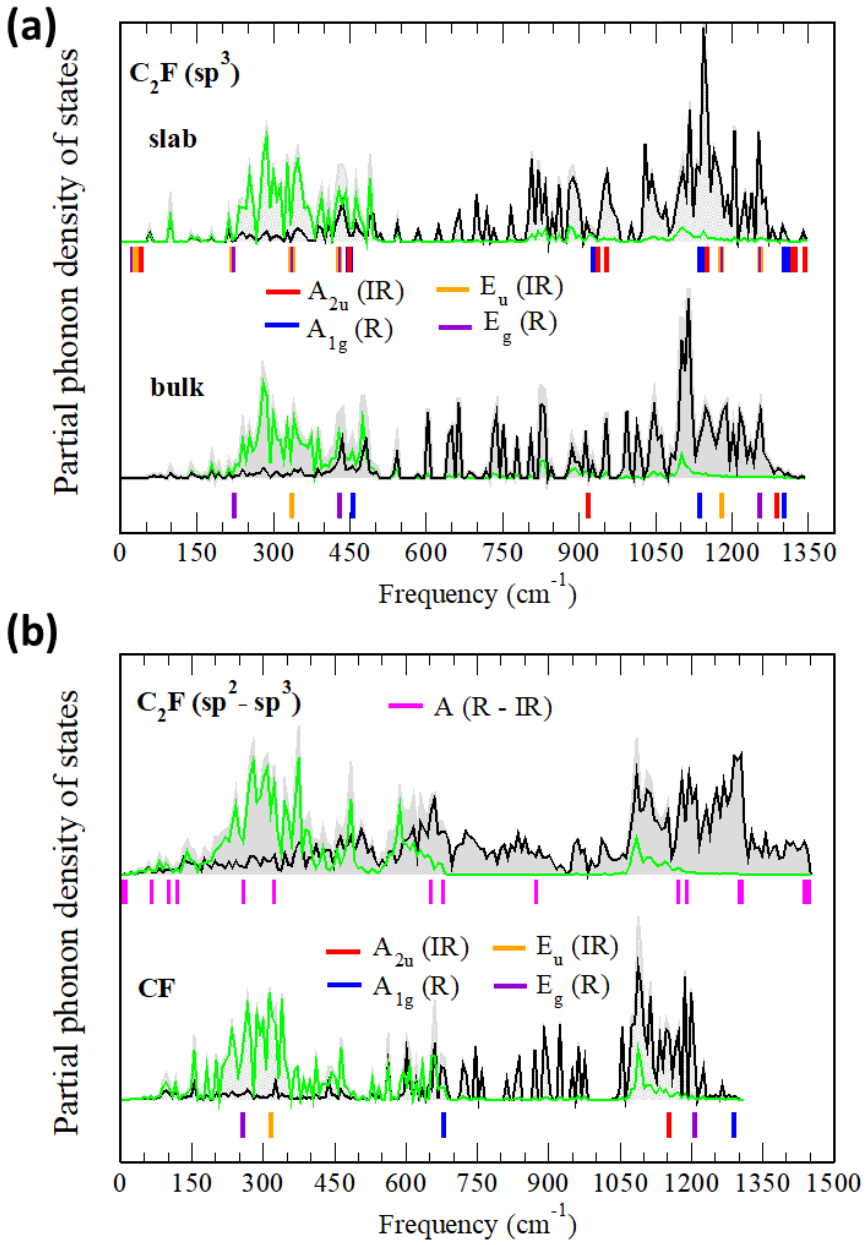

Figure 7. Contribution per species (green – fluorine atoms, black – carbon atoms and grey the sum of all contributions) of the phonon density of states calculated at 0 GPa. The ticks under the plot indicate the positions of the modes, color-coded for symmetry, as obtained for each structure.

IR spectroscopy is therefore an easy-to-use technique for distinguishing between $(C_2F)_n$ and $(CF)_n$ phases according to the intensities of the vibration bands at 1350 and 940 cm^{-1}. To go further, we reviewed the IR spectroscopy data of a set of materials; the data are

either published[61,66], from commercial product (ARC300 from ARC, USA, F/C = 0.83 from ^{13}C NMR), or synthesized for the comparison (from KS4 with different F/C, *i.e.* 0.61, 0.71 and 0.83; the fluorination temperatures were 380, 480 and 550 °C for 3 h in pure F_2). The non-published IR and ^{13}C NMR spectra are shown in Fig. S6a and b (IR and ^{13}C NMR data, respectively). The ratios of the intensities of the bands at 1350 (940) cm^{-1} and 1220 cm^{-1} are plotted as a function of the percentage of $(C_2F)_n$ phase (%$(C_2F)_n$ calculated from fit of ^{13}C NMR data) (Fig. 8). The data for pure $(CF)_n$ phase is fixed at zero for I_{1350}/I_{1220}, I_{940}/I_{1220} and %$(C_2F)_n$ (no line at 42 ppm). Both I_{1350}/I_{1220} and I_{940}/I_{1220} are linearly related to %$(C_2F)_n$ which definitely proves the assignment of the vibration lines to the $(C_2F)_n$ structural type. An IR spectrum is recorded in a few minutes with ATR mode, whereas NMR requires the equipment and several hours for a signal/noise ratio enough high to perform the fit for ^{13}C nuclei. As seen in the XRD part, this technique requires precaution to extract the relative contents of (C_2F) and $(CF)_n$ phases. Using the I_{1350}/I_{1220} versus %(C_2F) curve, those contents can be easily extracted. Nevertheless, the proposed method cannot be applied when residual graphitic phase is present and affects the baseline of the IR spectrum. Moreover, the line at 940 cm^{-1} is splitted into 2 components when sp^2 carbons are present in significant amount (see the typical examples of ARC3000 and $CF_{0.83}$ in Fig. S6b). I_{1350}/I_{1220} will be preferred than I_{940}/I_{1220} for the proposed method. In order to evidence the origin of the doublet for ARC3000 and $CF_{0.83,}$ fluorinated KS graphites with F/C ratio close to 0.8 and content of $(C_2F)_n$ in between 10 and 20 % were also considered (see FTIR spectra in Fig. SI7). The granulometry of the precursor for fluorination is different, *i.e.* 4, 6 and 15 μm grain size. The common point of this samples is a quite short fluorination duration (3 h) at 550°C in order to reach a F/C close to 0.8 (sub-fluorination). In all these samples as for ARC3000, $(C_2F)_n$ and $(CF)_n$ phases co-exist with residual carbon with sp^2 hybridization in significant amount (see the evidence by ^{13}C NMR in Fig. SI6a). This observation allows us to be exhaustive for the assignment of the

IR bands: the doublet is related to the coexistence of $(C_2F)_n$ and residual sp^2 carbons. Without one of these two components, the doublet is absent (FT_F-KS and FT_F-NG series).

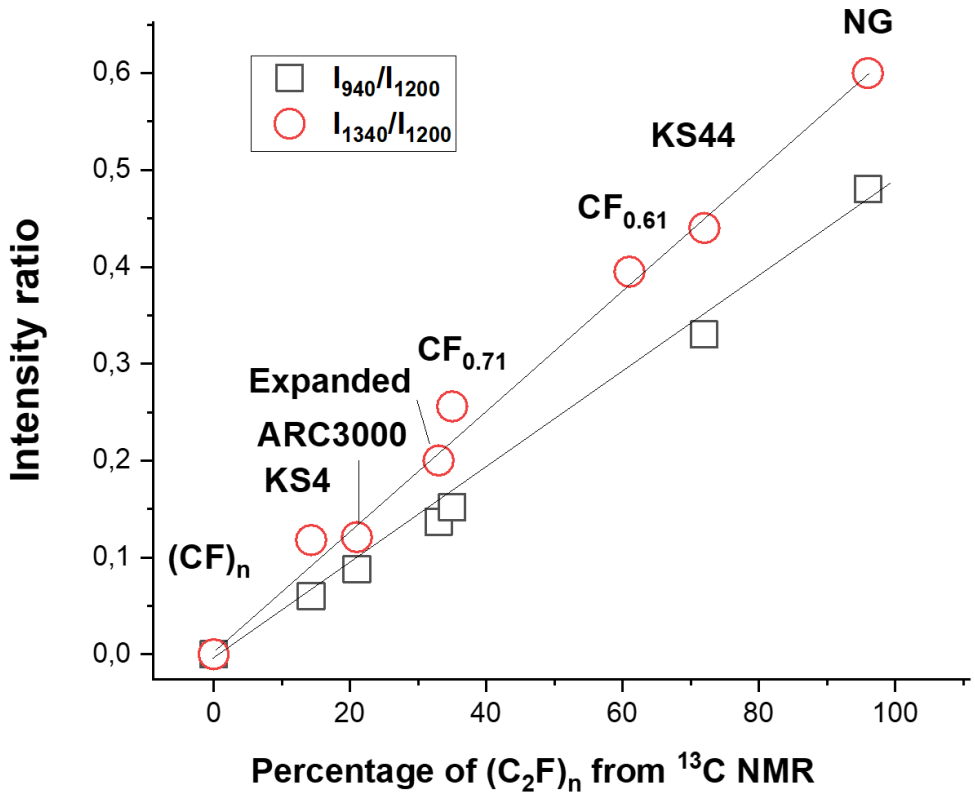

Figure 8. Correlation between IR vibration mode intensity, I_{1350}/I_{1220} and I_{940}/I_{1220}, versus %(C_2F) from ^{13}C NMR data. Data of $CF_{0.61}$ and expanded samples are extracted from references 59 and 66.

Two $(C_2F)_n$-rich samples with an interplanar distance *d* at least 9 Å, *i.e.* the maximum value for a covalent GF, were selected for neutron beam measurements, F440-NG and F450-KS with 96 % and 74 % of $(C_2F)_n$, respectively.

3.2 Compaction of the powdery graphite fluorinated samples

In order to avoid sample wrapping (and thus the effect of neutrons scattered by Teflon or other materials) and to explore future possibilities for scaling up fluorinated graphite as

neutron reflector, we investigated the compaction ability of the F450-KS powder by applying a pressure up to 1 GP at room temperature. The study is discussed in supplementary information (Appendix 2)

3.3 $(C_2F)_n$ phase as slow neutron reflector

We measured the differential macroscopic neutron scattering cross section $\frac{d\Sigma(\lambda_n)}{d\Theta}$ for two powdered samples of F450-KS (the density $\rho_{F450-KS} = 0.586\ g/cm^3$) and F440-NG ($\rho_{F440-NG} = 0.677\ g/cm^3$), as well as a sample graphite KS44 ($\rho_{KS44} = 0.337\ g/cm^3$), which was used to prepare the sample F450-KS. Strictly speaking, it consists of elastic and inelastic parts but the elastic part strongly dominates. Fig. 9 shows preliminary results on $\frac{d\Sigma(\lambda_n)}{d\Theta}$ for the KS44 (graphite, Fig. 9a) and the F450-KS (intercalated graphite, Fig. 9b) samples. The samples were not compressed or shaked to increase the density. Some effect of neutrons scattered on the Teflon packaging of the samples (~4.9 Å spacing, bright blue dashed lines in Fig. 9) and distortions at small scattering angles are not eliminated. The abscissa axes correspond to the scattering angle Θ. The ordinate axes correspond to the wavelength λ_n [in Å], the brightness corresponds to $\frac{d\Sigma(\lambda_n)}{d\Theta}$ [in $(cm \cdot degree)^{-1}$]. The blue and green solid lines show how the scattering peaks should occur on the crystal planes with the largest interplanar spacing, d_0 and for the d-space of the (100) plane in each sample; $d_{KS44} = 3.354$ Å and $d_{F450-KS} = 9.1$ Å.

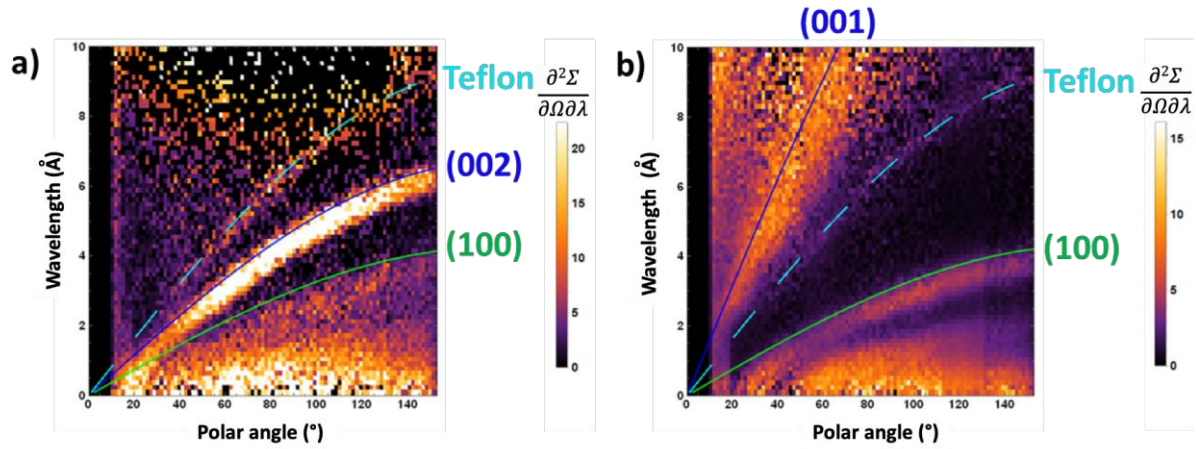

Figure 9. Differential macroscopic neutron scattering cross section $\frac{d\Sigma(\lambda_n)}{d\Theta}$ (mainly elastic) for KS44 (a) and F450-KS (b). Brightness corresponds to $\frac{d\Sigma(\lambda_n)}{d\Theta}$ [in $(cm \cdot degree)^{-1}$]. In blue and green, the scattering peaks of the largest interplanar spacing d_0 and d_{100}. Bright blue dashed lines indicate weak peaks from the Teflon packaging of samples.

Fig. 10 shows data on the total macroscopic cross section for neutron scattering in the angle range $10^o - 150^o$ for the three measured samples: F440-NG (black), F450-KS (red) and KS44 (blue). Scattering of neutrons into unmeasured angles will slightly increase the scattering cross sections, however, this effect is insignificant due to the relative smallness of the corresponding phase space elements, and might only improve the scattering efficiency.

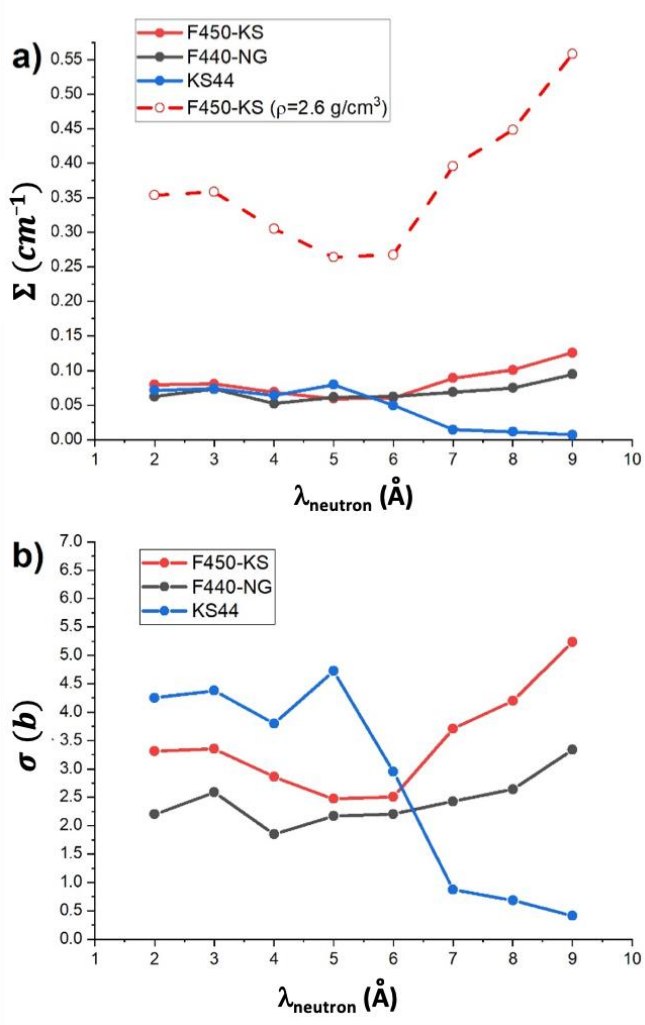

Figure 10. a) Total macroscopic scattering cross section in the angle range $10^o - 150^o$ for 3 samples: F450-KS (red), F440-NG (black) and graphite KS44 (blue). The sample densities are 0.586 g/cm^3, 0.677 g/cm^3 and 0.337 g/cm^3, respectively. The red dashed line shows the expected scattering cross section for F450-KS with the density of 2.6 g/cm^3 (the maximum achieved value after decompression, see Figure SI8). As clear from the comparison of solid red and dashed red curves, the density of F450-KS can strongly change as a function of the sample preparation procedure. Analysis of the results is in the text below. b) The same cross sections normalized to one atom.

Analysis of the results shown in Figure 10 allows us to draw several conclusions. Let's compare the results for the sample KS44, on the one hand, and the pair of samples F450-KS

and F440-NG, on the other hand. The cross section for neutron scattering on the sample KS44 drops sharply near (slightly lower than) the wavelength $\lambda_n^{Bragg(Gr)}$, as would be expected. Note that a slight scattering of neutrons with wavelengths $> \lambda_n^{Bragg(Gr)}$ is probably observed not on the sample itself, but on its Teflon holder (dashed lines if Figure 9). It cannot be eliminated completely by subtracting the results measured with an empty holder, because it is due to neutrons scattered first by the sample itself and then a second time by the holder. Apparently, the scattering of neutrons with wavelengths $> \lambda_n^{Bragg(Gr)}$ proper in the sample is negligible. The scattering of neutrons with wavelengths $< \lambda_n^{Bragg(Gr)}$ in samples F450-KS and F440-NG is approximately equal to the scattering in the starting graphite KS44, but at wavelengths $> \lambda_n^{Bragg(Gr)}$ the scattering increases to values even significantly exceeding the cross sections of neutrons with wavelengths $< \lambda_n^{Bragg(Gr)}$.

Reflectivity of F450-KS layers of different thicknesses is shown in Figure 11. It was simulated using the algebraic method for calculating neutron albedo. The method is similar to the diffusion approximation, but is valid in a wider region[71]. The measured differential elastic macroscopic neutron scattering cross section (Fig. 9) was used to calculate the corresponding transport cross sections. An account for a difference between elastic and total cross sections would decrease the calculated reflectivity, however, this effect is small and it's negligible is the reflector is cooled down. The cross section for neutron capture by nuclei was evaluated from the assumption that the F450-KS material consists only of carbon and fluorine in the structural phase of $(C_2F)_n$. Neutrons are isotropically incident on the surface of the flat layer, and during their interaction with the F450-KS material, only the processes of elastic neutron scattering and their capture by nuclei are taken into account.

It is important to note that the experimental differential elastic scattering cross section was measured in an incomplete range of polar scattering angles, from 10 to 150 °. This gives a lower limit in the albedo estimate, since additional neutron scattering in the angle ranges

from 0 to 10 ° and from 150 to 180 ° was not taken into account. However, as can be seen in Figure 9, the most intense broad Bragg diffraction peak for sample F450-KS does not exceed 110 ° in the wavelength range up to 10 Å. This means that the scattering of neutrons at large angles, which were not taken into account in the albedo calculation, has little effect on the transport cross section and, accordingly, the albedo due to the small number of such neutrons. Neutron scattering into the region of small angles up to 10 ° also affects the albedo insignificantly, since it makes a small contribution to the transport cross section by definition. Thus, we believe that the proposed approach allows us to reasonably estimate the albedo value. To more accurately calculate the reflectivity of F450-KS, it is necessary to explicitly take into account neutron scattering on the structural model of its crystal lattice. This would be a separate topic.

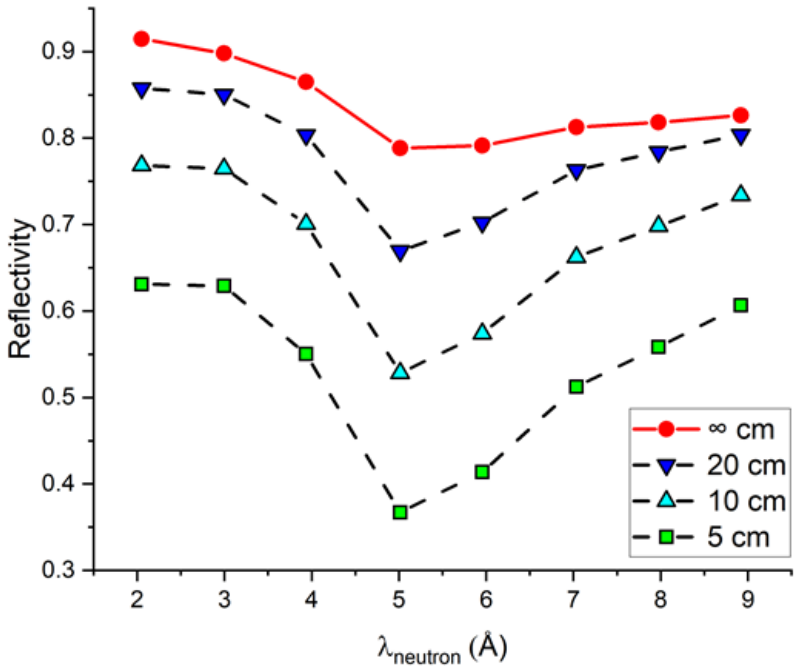

Figure 11. Calculated neutron albedo, as a function of wavelength $\lambda_{neutron}$, for the F450-KS layers of different thickness (5 cm (green squares), 10 cm (bright blue up triangle), 20 cm (blue down triangle), infinite (red)); the density is 2.6 g/cm^3.

Thus, 1) we confirmed the main initial hypothesis that graphite fluorides with $(C_2F)_n$ structural phase are efficient reflectors for neutrons with wavelengths $> \lambda_n^{Bragg(Gr)}$; 2) to characterize different graphite fluorides, as well as samples of other potentially interesting materials with large interplanar distances and low neutron losses, a specialized diffractometer developed as part of this work should be used, rather than standard diffractometers.

Let us now analyze the range of neutron wavelengths for which these conclusions are valid. At wavelengths of ~9 Å, the cross sections for neutron scattering from F450-KS and F440-NG samples continue to increase (or at least approach saturation) while the sensitivity of the diffractometer begins to drop sharply. This drop in sensitivity is due to several factors. Although the brightness of the neutron beam at the PF1B instrument has a record value[33], the neutron flux rapidly decreases with increasing neutron wavelength. Moreover, the small Li-rubber apertures (7 and 8 in Fig. SI1), required for working with small samples, further reduce the flux of the slowest neutrons. Finally, the maximum neutron flux that can be measured without dead-times and distortions by the BIDIM PSD detector is quite limited, and is determined by faster neutrons. Note that the problem of low sensitivity of the specialized diffractometer for the slowest neutrons can be significantly reduced in the future due to the appropriate shaping of the initial beam. For example, this can be done by isolating spectral bands with spectral shaping devices; one such device (the polarizer[70]) is a standard option at the PF1B instrument at ILL.

However, from the general knowledge of neutron diffraction by crystals, and also by analogy with the results shown in Fig. 10 for pristine graphite (KS44), we can confidently state that the range of effective neutron reflection from the $(C_2F)_n$ samples continues to values approximately equal to $\lambda_n^{Bragg(F450KS-KS)} = 2 \cdot 9.1$ Å ~18.2 Å. Direct measurements of scattering cross sections for wavelengths $\lambda_n > 9$ Å require further improvement of the

diffractometer. The range of neutron wavelengths and velocities for which poly(dicarbon monofluoride) $(C_2F)_n$ provides high efficiency of neutron reflection is shown in Fig. 12.

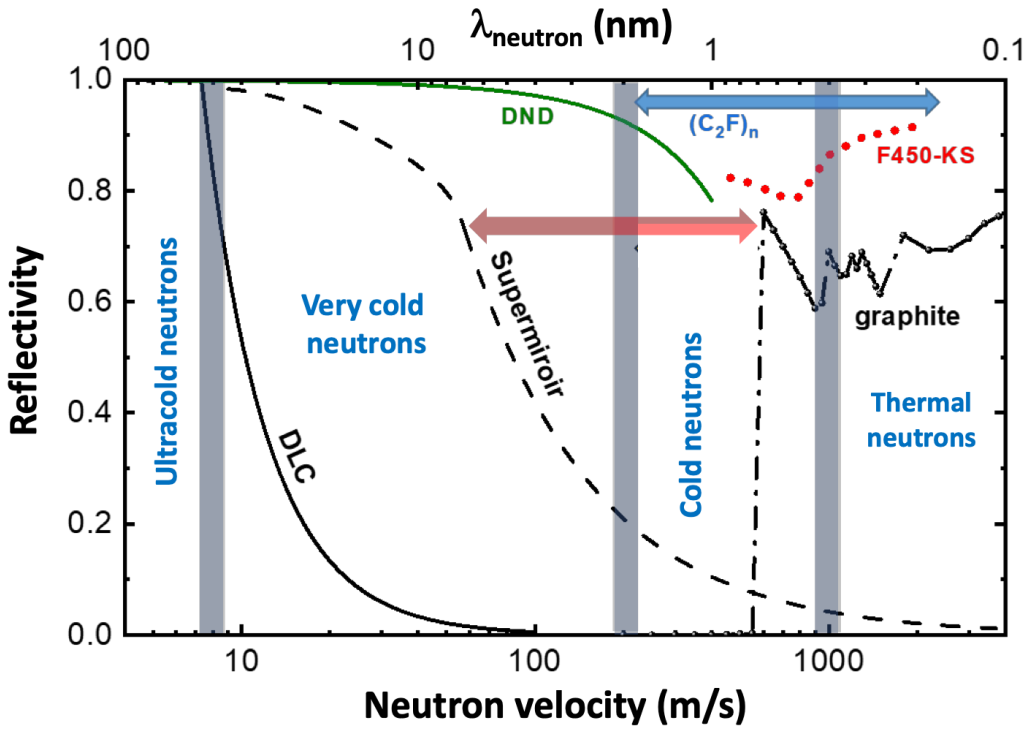

Figure 12. The elastic reflection probability for an isotropic neutron flux as a function of neutron velocity (bottom scale) and wavelength (top scale) for various carbon reflectors: 1) diamond-like coating (DLC) (solid line), 2) the best supermirror[68] (dashed line), 3) hydrogen-free DND powder of infinite thickness (green solid line), calculation, 4) calculation using the Monte Carlo N-Particle® (MCNP) standard program for reactor graphite reflector[69] with infinite thickness at ambient temperature (dashed-dotted line). Velocity (wavelength) ranges of ultracold, very cold, cold and thermal neutrons are separated by broad grey vertical lines. The range of neutron wavelengths and velocities for which Poly(dicarbon monofluoride) $(C_2F)_n$ provides high efficiency of neutron reflection is shown with blue arrow; the initial reflectivity gap is shown with red arrow, and the simulated neutron albedo in the measured range is shown with red dotted line (infinite F450-KS layer, the simplified model described above).

4. Conclusion

We have shown that $(C_2F)_n$-rich graphite fluoride can be used an efficient reflector for neutrons with wavelengths in the range $\lambda_n^{Bragg(Gr)} - \lambda_n^{F-DND} \cong 6 - 18$ Å and below, completely covering the gap in the reflectivity of modern neutron reflectors. To test this hypothesis, we have synthesized GF samples of different types, built a dedicated diffractometer to work with slower neutrons, and carried out a series of measurements using the neutron beam at the PF1B instrument in ILL, Grenoble, France, as well as a series of non-neutron methods for characterizing these samples. The measurements confirmed our assumptions and made it possible to make quantitative estimates. The most promising sample turned out to be $(C_2F)_n$ covalent graphite fluoride with the largest interplanar distance *d* of ~9 Å. This new type of reflectors is of significant interest, since they can make it possible for the first time to design neutron reflectors that are efficient in the full range of neutron wavelengths, to design neutron sources of a new type with unique parameters, to obtain record fluxes of cold and very cold neutrons. In order to overcome the difficulties for compaction of graphite fluoride powders, another strategy involves the use of graphite foils as starting material[72]. A detailed comparison of different intercalation modes is needed to optimize the efficiency of such reflectors, and a study of their radiation resistance is needed to assess the maximum radiation fluences/fluxes at which such reflectors can be practically used. The expected heating of the powder in the high radiation fluxes (gamma-quanta, fast neutrons etc), where such reflectors can be used, would not exceed about 100°C provided when a gaseous helium cooling is applied. The details of the cooling system (or its absence) largely depend on the concrete project. The thermal stability of graphite fluoride was extensively studied. In particular, the reference 73 gives the data for a graphite fluoride with $(C_2F)_n$ phase and a $CF_{0.57}$ composition. The decomposition of the C-F bonds in inert atmosphere starts at

520°C but most of them are broken around 580°C then far from the operating condition at 100°C thanks to He gas cooling (100°C).

Acknowledgements

This research was funded by ANR-20-CE08-0034 grant, France. The authors would like to thank the platforms “Microscopies, Microprobes and Metallography (3M)” and “X-Gamma” (Institut Jean Lamour, IJL, Nancy, France) for facilities access. S.R. gratefully acknowledges the Spanish Ministerio de Ciencia e Innovación (DOI: 10.13039/501100011033) under Projects PID2019-106383GB-C43 and PID2022-138076NB-C44. Neutron data were obtained from experiment doi:10.5291/ILL-DATA.3-07-409 at the PF1B instrument at ILL, Grenoble, France.

Supplementary Information

In attached file

References

1. I. Halpern, E. Fermi. Neutron Physics. s.l. : Los Alamos, 1946.
2 V.F. Sears, Neutron Optics. New York - Oxford : Oxford Univ. Press, 1989.
3. B.T.M. Willis, C.J. Carlile. Experimental Neutron Scattering. Oxford : Science, 2009.
4. A. Furrer, J. Mesot, Th. Strassle. Neutron Scattering in Condenced Matter Physics. London : World Scientific, 2009.
5. S. Esposito, O. Pisanti. Neutron Physics for Nuclear Reactors. Unpublished. Writings by Enrico Fermi. London : World Scientific, 2010.
6. D. Dubbers, M.G. Schmidt. The neutron and its role in cosmology and particle physics. Rev. Mod. Phys. 83 (2011) 1111. https://doi.org/10.1103/RevModPhys.83.1111
7. F.E. Wietfeldt, G.L. Greene. Colloquium: the neutron lifetime. Rev. Mod. Phys. 83 (2011) 1173. https://doi.org/10.1103/RevModPhys.83.1173
8. V.V. Nesvizhevsky, J. Villain. The discovery of the neutron and its consequences (1930–1940). Compt. Rend. Phys. 18 (2017) 592-600. https://doi.org/10.1016/j.crhy.2017.11.001
9. E. Fermi, Experimental production of a divergent chain reaction. Amer. J. Phys. S. 20 (1952) 536. https://doi.org/10.1119/1.1933322
10. W.H. Bragg, W.L. Bragg. The reflection of X-rays by crystals. Proc. Royal Soc. London A. 88 (1913) 428. https://doi.org/10.1098/rspa.1913.0040
11. M. Utsuro, K. Inaue. Bragg cutoff effects on neutron wave propagation in graphite. J. Nucl. Sci. Techn. 5 (1968) 298-308. https://doi.org/10.1080/18811248.1968.9732458
12. V.V. Nesvizhevsky, Interaction of neutrons with nanoparticles. Phys. At. Nucl. 65 (2002) 400-408.
13. V.V. Nesvizhevsky, E.V. Lychagin, A.Yu. Muzychka, A.V. Strelkov, G. Pignol, K.V. Protasov. The reflection of very cold neutrons from diamond powder nanoparticles. Nucl. Instr. Meth. A. 2008, 595 (2008) 631-636. https://doi.org/10.1016/j.nima.2008.07.149
14. E.V. Lychagin, A.Yu. Muzychka, V.V. Nesvizhevsky, G. Pignol, K.V. Protasov, A.V. Strelkov. Storage of very cold neutrons in a trap with nano-structured walls. Phys. Lett. B. 679 (2009) 186-190. https://doi.org/10.1016/j.physletb.2009.07.030
15. V. Nesvizhevsky, U. Koster, M. Dubois, N. Batisse, L. Frezet, A. Bosak, *et al*. Fluorinated nanodiamonds as unique neutron reflector. Carbon. 130 (2018) 799-805. https://doi.org/10.1016/j.carbon.2018.01.086
16. E. Lychagin, M. Dubois, V. Nesvizhevsky, Powders of diamond nanoparticles as a promising material for reflectors of very cold and cold neutrons. Nanomaterials 14 (2024) 387
17. A. Bosak, A. Dideikin, M. Dubois, J. Ivankov, E. Lychagin, A. Muzychka, *et al*. Fluorination of diamond nanoparticles in slow neutron reflectors does not destroy their crystalline cores and clustering while decreasing neutron losses. Mater. 13 (2020) 3337. https://doi.org/10.3390/ma13153337
18. A. Aleksenskii, M. Bleuel, A. Bosak, A. Chumakova, A. Dideikin, M. Dubois, *et al*. Effect of particle sizes on the efficiency of fluorinated nanodiamond neutron reflectors. Nanomater. 11 (2021) 3067. https://doi.org/10.3390/nano11113067
19. A. Aleksenskii, M. Bleuel, A. Bosak, A. Chumakova, A. Dideikin, M. Dubois, *et al*. Clustering of diamond nanoparticles, fluorination and efficiency of slow neutron reflectors. Nanomater. 11 (2021) 1945. https://doi.org/10.3390/nano11081945
20. J.R. Granada, J.I.M. Damian, J. Dawidowski, J.I. Robledo, C. Helman, G. Romanelli, *et al*. Development of neutron scattering kernels for cold neutron reflector materials. J. Neutron Res. 23 (2021) 167.
21. V.V. Nesvizhevsky, V. Gudkov, K.P. Protasov, W.M. Snow, A.Y. Voronin. Experimental Approach to Search for Free Neutron-Antineutron Oscillations Based on Coherent Neutron and Antineutron Mirror Reflection. Phys. Rev. Lett. 122 (2019) 221802. https://doi.org/10.1103/PhysRevLett.122.221802
22. V. Nesvizhevsky, V. Gudkov, E. Kupryanova, K. Protasov, M. Snow, A. Voronin. Implementations of neutron/antineutron guides in experiments searching for neutron-antineutron oscillations. PARTICLES AND Nuclei International Conference 2021, PANIC2021. 2021, 428.
23. V Nesvizhevsky,. Why very cold neutrons could be useful for neutron-antineutron oscillation searches. J. Neutr. Res. 2022, S. 24: 223-227. https://doi.org/10.3233/JNR-220003
24 V.V. Nesvizhevsky, G. Pignol, K.V. Protasov. Neutron scattering and extra short range interactions. Phys. Rev. D. 77 (2008) 034020. https://doi.org/10.1103/PhysRevD.77.034020
25. W.M. Snow, C. Haddock, B. Heacock. Searches for exotic interactions using neutrons. Symmetry. 14 (2022) 10. https://doi.org/10.3390/sym14010010
26. Mezei, F. Neutron spin echo: A new concept in polarized thermal neutron techniques. Z. Phys. 255 (1972) 146-160. https://doi.org/10.1007/BF01394523

27. M. Hino, S. Tasaki, Y. Kawabata, T. Elisawa, P. Geltenbort, T. Brenner, *et al*. Development of a very cold neutron spin interferometer at the ILL. Phys. B. 2003, 335 (2003) 230-233. https://doi:10.1016/S0921-4526(03)00244-8
28. T. Oda, M. Hino, M. Kataguchi, H. Filter, P. Geltenbort, Y. Kawabata,. Towards a high-resolution TOF-MIEZE spectrometer with very cold neutrons. Nucl. Instr. Meth. A. 860 (2017)35-41. https://doi:10.1016/j.nima.
29 A.I. Ioffe, Diffraction grating interferometer for very cold neutrons. Nucl. Instr. Meth. 1984, 204: 565.
30. J. Baumann, R. Gahler, J. Kalus, W. Mampe. Experimental limit for the charge of the free neutron. Phys. Rev. D. 37 (1988) 3107. https://doi.org/10.1103/PhysRevD.37.3107
31. Maruyama, R. Cold and very cold neutron radiography for high contrast neutron imaging in kyoto university reactor. J. Radioanal. Nucl. Chem. 264 (2005) 319-324. https://doi.org/10.1007/s10967-005-0714-9
32. V.V. Nesvizhevsky, A.O. Sidorin. Production of ultracold neutrons in a decelerating trap. J. Neutr. Res. 24 2022193-204. https://doi.org/10.3233/JNR-220006
33. H. Abele, D. Dubbers, H. Hase, M. Klein, A. Knopfler, M. Kreuz, *et al*. Characterization of a ballistic supermirror neutron guide. Nucl. Instr. Meth. A. 562 (2006) 407-417. https://doi.org/10.1016/j.nima.2006.03.020
34. K. Shen, X. Chen, W. Shen, Z.-H. Huang, B. Liu. Thermal and gas purification of natural graphite for nuclear. Carbon. 173 (2021) 769. https://doi.org/10.1016/j.carbon.2020.11.062
35. C. Cavallari S. Radescu, M. Dubois, N. Batisse, H. Diaf, V. Pischedda, Tuning C-F bonding of graphite fluoride by applying high pressure: experimental and theoretical study. J. Phys. Chem. C 124 (2020) 24747–24755 https://doi.org/10.1021/acs.jpcc.0c06860
36. N. Watanabe, T. Nakajima, R. Hagiwara, Discharge reaction and overpotential of the graphite fluoride cathode in a nonaqueous lithium cellJ. Power Sources 20 (1987) 87-92. https://doi.org/10.1016/0378-7753(87)80095-2
37. H. Groult, A. Tressaud, Use of inorganic fluorinated materials in lithium batteries and in energy conversion systems. Chem. Commun. 54 (2018) 11375- 11382. https://doi.org/10.1039/C8CC05549A
38. N. Watanabe, T. Nakajima, H. Touhara, Graphite Fluorides, Vol. 8, Elsevier, Amsterdam 1988;
39. T. Nakajima, N. Watanabe, in Graphite, Fluorides, and Carbon- Fluorine Compounds, Vol. 84, CRC Press, Boca Raton, FL 1991.
40. H. Touhara, F. C. Okino, Property control of carbon materials by fluorination. Carbon 38 (2000) 241-267. https://doi.org/10.1016/S0008-6223(99)00140-2
41. Y. Sato, K. Itoh, R. Hagiwara, T. Fukunaga, Y. Ito, Short-range structures of poly(dicarbon monofluoride) (C2F)n and poly(carbon monofluoride) (CF)n). Carbon 42 (2004) 2897-2903. https://doi.org/10.1016/j.carbon.2004.06.042.
42. A. Hamwi, M. Daoud, J. C. Cousseins, New graphite fluorides as electrode materials in lithium batteries J. Power Sources 27 (1989) 81-87. https://doi.org/10.1016/0378-7753(89)80107-7
43. M. Dubois, K. Guerin, J. P. Pinheiro, F. Masin, Z. Fawal, A. Hamwi, NMR and EPR studies of room temperature highly fluorinated graphite heat-treated under fluorine atmosphereCarbon 42 (2004) 1931-1940. https://doi.org/10.1016/j.carbon.2004.03.025
44. K. Guérin, J. P. Pinheiro, M. Dubois, Z. Fawal, F. Masin, R. Yazami, *et al*, Synthesis and Characterization of Highly Fluorinated Graphite Containing sp2 and sp3 Carbon. Chem. Mater. 16 (2004) 1786-1792. https://doi.org/10.1021/cm034974c
45. Y. Sato, K. Itoh, R. Hagiwara, T.Fukunaga, Y. Ito, On the so-called “semi-ionic” C–F bond character in fluorine–GIC, Carbon, 42 (2004) 3243-3249, https://doi.org/10.1016/j.carbon.2004.08.012
46. O. Ruff, O. Bretschneider, Die Reaktionsprodukte der verschiedenen Kohlenstoffformen mit Fluor II (Kohlenstoff-monofluorid), Zeitschrift für anorganische und allgemeine Chemie. 217 (1934) 1–18. https://doi.org/10.1002/zaac.19342170102.
47. W. Rüdorff, G. Rüdorff Graphite Intercalation Compounds, in: H.J. Emeléus, A.G. Sharpe (Eds.), Advances in Inorganic Chemistry and Radiochemistry, Academic Press, 1959, 223–266. https://doi.org/10.1016/S0065-2792(08)60255-1.
48. Y. Kita, N. Watanabe, Y. Fujii, Chemical composition and crystal structure of graphite fluoride, J. Am. Chem. Soc. 101 (1979) 3832–3841. https://doi.org/10.1021/ja00508a020.
49. Kita et al, Solid State Ionics 1 (1980) 87–110
50. V. Pischedda, S. Radescu, M. Dubois, N. Batisse, F. Balima, C. Cavallari, *et al*. Experimental and DFT high pressure study of fluorinated graphite (C2F)n, Carbon, 114 (2017), 690-699. 10.1016/j.carbon.2016.12.051
51. G. Kresse, J. Hafner Ab initio molecular dynamics for liquid metals. Phys. Rev. B: Condens. Matter Mater. Phys. 1993, 47, 558. doi:10.1103/PhysRevB.47.558
52. G. Kresse, J. Furthmüller Efficiency of ab-initio total energy calculations for metals and semiconductors using a plane-wave basis set. Comput. Mater. Sci. 1996, 6, 15. doi: 10.1016/0927-0256(96)00008-0
53. G. Kresse, J. Furthmüller Efficient iterative schemes for ab initio total-energy calculations using a plane-wave basis set. Phys. Rev. B: Condens. Matter Mater. Phys. 54 (1996) 11169. For more information see: http://cms.mpi.univie.ac.at/vasp doi:10.1103/PhysRevB.54.11169

54. J.P. Perdew, *et al*., Restoring the density-gradient expansion for exchange in solids and surfaces, Phys. Rev. Lett. 100 (13) (2008) 136406, https://doi.org/10. 1103/PhysRevLett.100.136406
55. S. Grimme J. Antony, S. Ehrlich, H. Krieg. A Consistent and Accurate Ab Initio Parametrization of Density Functional Dispersion Correction (DFT-D) for the 94 Elements H-Pu. The Journal of Chemical Physics 132 (2010) 154104, doi:10.1063/1.3382344
56. A. Togo, I. Tanaka, First principles phonon calculations in materials science, Scripta Mater. 108 (2015) 1e5, https://doi.org/10.1016/j.scriptamat. 2015.07.021.
57. T. Mallouk, N. Bartlett, Reversible intercalation of graphite by fluorine: a new bifluoride, C12HF2, and graphite fluorides, CxF (5 > x > 2) J. Chem. Soc., Chem. Commun. (1983) 103-105. https://doi.org/10.1039/C39830000103
58. T. Mallouk, B. L. Hawkins, M. P. Conrad, K. Zilm, G. E. Maciel, N. Bartlett, Raman, infrared and n.m.r. studies of the graphite hydrofluorides CxF1-δ(HF)δ($2 \leq x \leq 5$) Philos. Trans. R. Soc. 314 (1985) 179. https://doi.org/10.1098/rsta.1985.0017
59. M. Dubois, J. Giraudet, K.Guérin, A.Hamwi, Z. Fawal, P.Pirotte, *et al.*, EPR and Solid-State NMR Studies of Poly(dicarbon monofluoride) (C2F)n J. Phys. Chem. B 110 (2006) 11800–11808. https://doi.org/10.1021/jp061291m
60. J. Giraudet, M. Dubois, K. Guérin, C. Delabarre, A. Hamwi, F. Masin, Solid-State NMR Study of the Post-Fluorination of (C2.5F)n Fluorine−GIC J. Phys. Chem. B 111 (2007) 14143-14151. https://doi.org/10.1021/jp076170g
61. M. Dubois, J. Giraudet, K. Guérin, A. Hamwi, Z.Fawal, P.Pirotte, EPR and Solid-State NMR Studies of Poly(dicarbon monofluoride) (C2F)n *et al.*, J. Phys. Chem. B 110 (2006) 24, 11800–11808
62. J. Giraudet, M. Dubois, K. Guérin, C. Delabarre, A. Hamwi, F. Masin, J. Phys. Chem. B 111 (2007) 14143.
63. Y. Kita, N. Watanabe, Y. Fujii. Chemical Composition and Crystal Structure of Graphite Fluoride. J. American Chem. Soc. 101 (1979) 3832 41. https://doi.org/10.1021/ja00508a020.
64. Y. Sato, K. Itoh, R. Hagiwara, T. Fukunaga, Y. Ito. Short-range structures of poly(dicarbon monofluoride) (C2F)n and poly(carbon monofluoride) (CF)n. Carbon 42 (2004) 2897 2903. https://doi.org/10.1016/j.carbon.2004.06.042.
65. H. Touhara, K. Kadono, Y. Fujii, N. Watanabe, On the Structure of Graphite Fluoride, Z. Anorg. Allg. Chem. 544 (1987) 7–20. https://doi.org/10.1002/zaac.19875440102.
66. M. Colin, X. Chen, M. Dubois, A. Rawal, D.J. Kim, F-diamane-like nanosheets from expanded fluorinated graphite, Applied Surface Science. 583 (2022) 152534. https://doi.org/10.1016/j.apsusc.2022.152534.
67. V. Pischedda, S. Radescu, M. Dubois, C. Cavallari, N. Batisse, F. Balima et al. Carbon, 127 (2018) 384-391 ttps://doi.org/10.1016/j.carbon.2017.10.094
68. C. Schanzer, M. Schneider, P. Boni, Neutron optics: towards applications for hot neutrons. J. Phys. Conf. Ser. 746 (2016) 012024. https://doi.org/10.1088/1742-6596/746/1/012024
69. Fermi, E. A course in neutron physics in Collected papers. Publisher: The University of Chicago Press, Chicago, 1965
70. A.K. Petoukhov, V.V. Nesvizhevsky, T. Bigault, P. Courtois, A. Devishvili, D. Jullien, *et al.*, Realization of an advanced super-mirror solid-state neutron polarizer for the instrument PF1B at the Institut Laue-Langevin, Rev. Sci. Instr. 94 (2023) 023304. https://doi.org/10.1063/5.0123419
71. V. K. Ignatovich and E. P. Shabalin, 'Algebraic method for calculating a neutron albedo', Phys. At. Nucl., 70, 2 (2007) 265–272. https://doi.org/10.1134/S106377880702007X
72. K. Henry, M. Colin, G. Chambery, B. Vigolo, S. Cahen, C. Hérold, et al Flexible fluorinated graphite foils with high content of (C2F)n phase for slow neutron reflector, Dalton Tans, 2024, Accepted Manuscript https://doi.org/10.1039/D4DT00794H
73. M. Dubois, K. Guérin, Y. Ahmad, N. Batisse, M. Mar, L. Frezet, et al, Thermal exfoliation of fluorinated graphite, Carbon, 77 (2014) 688-704. https://doi.org/10.1016/j.carbon.2014.05.074.